Microsc. Microanal. 17, 410–417, 2011
doi:10.1017/S1431927611000183

Microscopy AND Microanalysis

Bridging the Micro-to-Macro Gap: A New Application for Micro X-Ray Fluorescence

Jeffrey M. Davis,[1]* Dale E. Newbury,[1] Albert Fahey,[1] Nicholas W.M. Ritchie,[1] Edward Vicenzi,[1] and Dale Bentz[2]

[1]*National Institute of Standards and Technology, Microanalysis Research Group, 100 Bureau Drive, Gaithersburg, MD 20899-8371, USA*
[2]*National Institute of Standards and Technology, Materials and Construction Research Division, 100 Bureau Drive, Gaithersburg, MD 20899-8371, USA*

Abstract: X-ray elemental mapping and X-ray spectrum imaging are powerful microanalytical tools. However, their scope is often limited spatially by the raster area of a scanning electron microscope or microprobe. Limited sampling size becomes a significant issue when large area (>10 cm^2), heterogeneous materials such as concrete samples or others must be examined. In such specimens, macro-scale structures, inclusions, and concentration gradients are often of interest, yet microbeam methods are insufficient or at least inefficient for analyzing them. Such requirements largely exclude the samples of interest presented in this article from electron probe microanalysis. Micro X-ray fluorescence–X-ray spectrum imaging (μXRF-XSI) provides a solution to the problem of macro-scale X-ray imaging through an X-ray excitation source, which can be used to analyze a variety of large specimens without many of the limitations found in electron-excitation sources. Using a mid-sized beam coupled with an X-ray excitation source has a number of advantages, such as the ability to work at atmospheric pressure and lower limits of detection owing to the absence of electron-induced bremsstrahlung. μXRF-XSI also acts as a complement, where applicable, to electron microbeam X-ray output, highlighting areas of interest for follow-up microanalysis at a finer length scale.

Key words: imaging, mapping, analysis, concrete, meteorites, elemental

Introduction

For more than 40 years, elemental mapping has proven to be among the most popular methods of characterizing compositional microstructure with electron-excited X-ray spectrometry. It is commonly practiced by researchers using the electron probe microanalyzer (EPMA) or the analytical scanning electron microscope (SEM), with wavelength dispersive spectrometry (WDS) and/or energy dispersive X-ray spectrometry (EDS) (Cosslett & Duncumb, 1956). EPMA/SEM elemental mapping is capable of submicrometer lateral resolution (depending on the material chemistry and electron beam energy), so the field width of the analyzed area typically ranges from 10 μm to 2 mm. However, the analyst is often confronted with the additional need to examine compositional variations over large areas with lateral dimensions of centimeters. The maximum area accessible for elemental mapping under conventional electron beam scanning conditions is limited by the angular sweep for the electron beam at maximum deflection at a particular working distance suitable for EDS or WDS analysis. For example, a minimum image magnification may correspond to a horizontal field width of approximately 2.5 mm. A further limitation on the maximum X-ray mapping area may be imposed by spectrometer X-ray defocusing for WDS or decollimation effects for EDS. When larger areas are interrogated, the analyst must either be prepared to tile perhaps hundreds of maps, or alternatively, use the method of mechanical stage scanning with a fixed beam. Ideally, the mapping area for stage scanning is limited by the ultimate range of the stage motion, though the practical mapping area is often defined by chamber design limitations. Moreover, by fixing the beam and moving the specimen, WDS defocusing and EDS collimation limits are avoided because the excited region of the specimen is always brought to the optimum focus/collimation point for the spectrometer.

Issues of practicality often arise when producing stage scanned X-ray images with WDS spectrometers. First, despite the ability to defocus the electron beam to diameters well over 50 μm, the narrow acceptance angles of WDS spectrometers, depending on crystal type and spectrometer geometry, significantly limit the lateral resolution of the generated X-rays. The end result is often significant undersampling for stage maps, as the time penalty for large stage maps is particularly severe for small (<40 μm) probe sizes. It should be noted that the time penalty for stage mapping is a mechanical issue, not directly related to the excitation source. Second, the flatness requirement for high accuracy WDS requires samples to have extremely low surface roughness and to be parallel with the scanning plane. While a surface with some slope in the scanning plane could be corrected with linear interpolation between corner points, not all large samples have perfectly linear slope features. The ability to produce large samples that are both smooth

Received August 18, 2010; accepted January 31, 2011
*Corresponding author. E-mail: jeff.davis@nist.gov

and flat is often limited to those with extreme patience and high quality polishing equipment. While rough, tilted samples are also an issue for EDS analysis—due largely to deviation from take-off angle—the errors induced by surface topology are smaller when compared to WDS. Finally, the entire sample, after preparation, must be capable of being subjected to high vacuum, both for analysis and for possible carbon coating.

Focused-beam X-ray fluorescence (XRF) performed with a commercial, laboratory-scale instrument has recently emerged as an alternative for large area mapping. XRF is classically performed with a large area beam (millimeters to centimeters) as a bulk analysis technique. The emergence of capillary X-ray optics, which focus X-ray beams by multiple reflections off the inner surface of a tapered glass capillary or cluster of capillaries, has enabled the production of an X-ray beam focused to a diameter of 100 μm or finer from a modest, laboratory-scale X-ray tube source (Gurker, 1986; Nichols et al., 1987; Carpenter, 1989). Such a beam diameter is useful for mapping on a large spatial scale where the basic pixel step is matched to the beam size (Boehme, 1987; Carpenter & Taylor, 1991). Although smaller beams are routinely achieved at synchrotron sources, which may truly deserve the "micro" designation, the industry and accepted literature still refers to μXRF (Adams et al., 1998).

In terms of imaging and trace element analysis, polychromatic X-ray beam sources have a significant advantage over their electron beam counterparts (Havrilla, 1997). Secondary characteristic X-rays are generated following photoelectric ionization of sample atoms by primary X-ray photons. The photoelectric absorption process has its highest cross section for photons that just exceed the critical excitation (edge) energy for a particular atomic shell of the specimen atom. As the primary photon energy increases above the edge energy, the ionization cross section decreases. Thus, by having the primary X-ray continuum, there are primary X-ray photons of the appropriate energy to excite all ionization edges across the full analytical range, which gives μXRF broad elemental coverage. For energetic photons (>10 keV), the μXRF detection limits are considerably lower, and the peak-to-background ratios are higher than those recorded in the electron beam instrument. Of course, where the anode material characteristic X-ray peaks occur, the primary intensity is increased over the continuum intensity.

Early μXRF systems were only capable of collecting X-ray intensity maps, commonly called region of interest maps, where the raw X-ray count intensity in preset windows was recorded, and the remaining spectral information was lost (Rindby et al., 1989). This operational compromise was primarily due to the limitations of personal computers available at the time of the first generation μXRF instruments. In recent years, hard drive capacity and processor speed have allowed analysts to operate in the X-ray spectrum imaging (XSI) mode in which a complete 4,096 channel (10 eV channel width) spectrum is recorded at each beam location, often resulting in 1 GB or larger data cubes for even modest pixel density spectrum images. Such data cubes can now be efficiently interrogated using a variety of software packages, including the National Institute of Standards and Technology (NIST) Lispix and Sandia's Axsia program (Bright, 2000; Kotula et al., 2003). It is this combination of X-ray spectrum imaging and stage scanning that makes this technique a viable solution to the micro-to-macro problem.

The summation of difficulties for measuring large area specimens in an SEM or EPMA system is the "micro-to-macro" problem. In specimens where variations in composition occur over centimeters, it is difficult to track and measure the variations when limited to a relatively small portion of the sample. For broader applications, any heterogeneous sample should be interrogated in its entirety to ensure that any microstructural investigation is representative of the sample as a whole. The solution to the micro-to-macro problem may be stated simply as using a larger beam so as to efficiently interrogate large specimens. Specific to μXRF, the advantage of using an X-ray beam, as opposed to an electron or ion beam, is the ability to work nondestructively, at modest vacuum, over rough samples, without the need for a conductive coating. Moreover, μXRF-XSI complements SEM-EPMA spectral imaging with the special attributes of XRF analysis, which will be further demonstrated and discussed below. While EPMA is not necessarily inferior to μXRF-XSI, this article intends to establish materials and methods where μXRF-XSI provides a useful complement to an already well-established technique. Additionally, this article provides three examples wherein both X-ray images and spectra are required to gain a complete understanding of the material, thereby using the full advantages of X-ray spectrum imaging.

Experimental Method

For illustrative purposes, the instrument used in this work is an EDAX (Mahwah, NJ, USA) Eagle III μXRF system.[a] The system uses a liquid nitrogen cooled Si(Li) energy dispersive spectrometer and focuses the X-rays from a Rh target (excitation potential to 40 kV) with a polycapillary optic designed by X-ray Optical Systems, Inc. (East Greenbush, NY, USA). Stage motion is controlled by stepper motors with a position reproducibility of approximately ± 3 μm (1 standard deviation). As shown in the schematic of Figure 1, the focused X-ray beam is incident to the sample at a 65° angle from the horizontal, while the take-off angle of the EDS detector is 60° above the horizontal plane.

A series of measurements of the EDAX Eagle III μXRF system has been performed to better understand the nature of the measurement system. For the specific application of imaging, two factors are of greatest importance. The first factor is the lateral sampling area, defined as the area from which a significant portion of the X-rays are produced. The

[a]Certain commercial equipment, instruments, and materials, or software are identified in this article to specify adequately the experimental procedure. Such identification does not imply recommendation or endorsement of these items by the NIST, nor does it imply that they are the best available for the purpose.

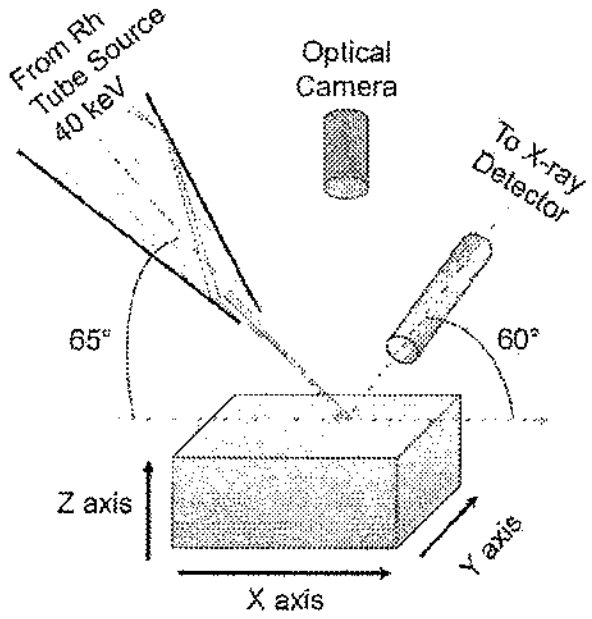

Figure 1. Schematic diagram of an Eagle III μXRF system. The schematic shows the relative positions of the detector, camera, and X-ray source in the μXRF system. It also provides a reference for sample orientation. Note that the elements in the schematic are not to scale.

second factor is the beam stability, defined as the change in detected X-ray intensity over time. To measure the lateral sampling area, a line profile (stage mapping under a stationary beam) was recorded across a Cu/Zn interface. The interface was created by electroplating copper onto the zinc, so that interdiffusion was minimized to produce a sharp interface. To reduce the secondary fluorescence of zinc on copper, the interface was held parallel to the line joining the excited sample volume and the detector face such that the detection path for Zn X-rays did not pass through copper. Results from this experiment are shown as Figure 2, with the k-ratios derived using Desktop Spectrum Analyzer II (DTSA II) to process the data (Ritchie, 2008). The step distance across the profile from 86% to 14% of the pure elemental standard is recorded, the lateral sampling area is calculated as 52 μm ± 4 μm (1 standard deviation). In this measurement, error was determined by fitting a Gaussian curve to an average of three replicate analyses. The summation of fitting error along with error induced by stage reproducibility and counting statistics made up the error budget for the experiment. The 86% to 14% values were selected as approximately $1 - 1/e^2$ and $1/e^2$, and they represent a region of approximate linearity when analyzing sigmoidal curves. A possible alternative is to look at the region enclosed by 2σ, or a range of 95% to 5% of the pure

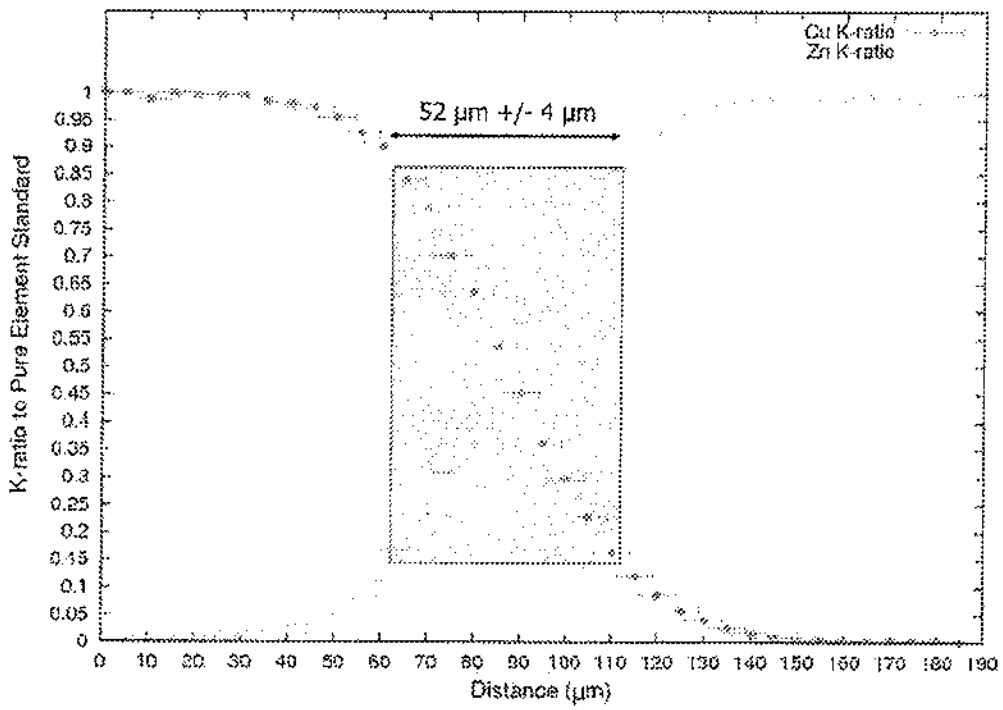

Figure 2. K-ratios derived from scanning across a Cu/Zn interface. This chart shows the variance of K-ratios as an electroplated Cu-Zn interface is scanned underneath the X-ray beam. Data points represent an average of three measurements, with x error bars showing precision of the stage and y error bars showing reproducibility of the K-ratio measurements. K-ratios were calculated using NIST DTSA II with pure elemental standards and a multiple linear least-squares fit. The area representing the 86/14 signal intensity is shown in the hatched gray box, and its width is calculated as 52 μm ± 4 μm. Fitting a Gaussian model to both the Cu and Zn curves shows that the data are well modeled by a Gaussian curve ($R^2 = 0.95$). It should be noted that the experiment was done with 100 μA of current, and that the apparent lateral sampling area increases slightly with increasing current.

element standard intensity. To measure the signal stability, an automated collection of 500 spectra on a homogeneous, pure (>99.99% SiO_2) SiO_2 glass was completed. The integrated peak intensity of the Si_{K-L2} (Si Kα) peak was plotted against the total time of the analysis. A linear regression confirms that the loss of signal intensity occurs at approximately 0.020% ± 0.001% per hour during the 18 h period. Results from this experiment are shown in Figure 3. Overall, the stability of X-ray tube is excellent, and in some cases it exceeds the signal stability found in electron probe instruments.

The most important factors of mapping strategy are the size of the area to be covered, the number of pixels, and the pixel dwell time, which together determine the time needed to acquire an X-ray spectrum image at a given uncertainty. The pixel dwell time, defined as the time X-rays are collected from the sample for a given location, should be chosen to optimize the requirements of counting statistics and reasonable instrument use. When pixel dwell times are too short, instrument overhead becomes a significant portion of the runtime, and counting uncertainties are frequently high for elements of interest. As is the case with both electron and X-ray excited spectrum imaging, low counting statistics produce images where the variability in intensity is too high for compositional analysis. While long pixel dwell times will provide high precision and improve detection of trace elements, the time penalty for specimens of centimeter dimensions is significant. Given that analysts in the microanalysis field, through the implementation of silicon drift detectors, are accustomed to mapping times of only a few hours, most labs may not be able to make the 24 to 60 h time commitment for a large area map.

A common approach in determining the step size is to divide the area to be measured by the lateral sampling area or nominal beam size. However, in practice, these values do not fully account for the beam spread normally seen with polycapillary optics. Taking into account the full tailing of the X-ray intensities shown in Figure 2 down to only 5% of signal intensity, the lateral sampling area is nearly 100 μm. In addition, significant oversampling (i.e., pixel spacing less than half the nominal beam diameter) does little to improve image quality. Practice has shown that step sizes approximately 1.5 times the lateral sampling area (measured using values of $1/e^2$, as mentioned above) gives sufficient resolution for imaging large areas, while allowing for enough dwell time per pixel within reasonable time constraints.

Results and Discussion

Comparison of X-Ray-Excited and Electron-Excited EDS

To show the particular strength of X-ray excited EDS, a sample of homogeneous NIST microanalysis glass K2380 was analyzed in both the μXRF and in a conventional SEM. The glass was selected because it contained trace amounts of uranium (L_3-$M_{4,5}$ = 13.6 keV) and thorium (L_3-$M_{4,5}$ = 13.0 keV), which are difficult to analyze due to high excitation voltage and high bremsstrahlung in electron excited systems. As shown in the comparison of μXRF and electron-excited spectra in Figure 4 for glass K2380 (a glass created at NIST for internal use by Kaufman), the μXRF has a significantly higher peak-to-background ratio for elemental peaks in the region from 5 to 15 keV, which leads to lower limits of detection by a factor of 5 to 10 compared to electron-excited spectra. The lower relative background of the μXRF spectrum is a particular advantage when minor and trace elements are of interest.

Large Feature Imaging

The first of three examples shown in this article as case studies for large area X-ray mapping is an example from the cement and concrete industry. Chloride ions are widely recognized as dangerous to reinforced concrete structures (ACI-222, 1996). As chloride ions, supplied by natural sources or from deicing salts applied during winter months, infiltrate into the concrete, they cause the reinforcing steel to rust. Rusted reinforcing steel drastically decreases both the strength and the service life of concrete structures and can even cause catastrophic failures of prestressed structures (Monfore & Verbeck, 1960). The simplest method for measuring the depth of infiltration of chloride ions is to spray an exposed cross section of concrete with a solution of silver nitrate ($AgNO_3$) (Collepardi et al., 1970). Silver chloride (AgCl) will precipitate out, forming a light gray film wherever chloride ions are present. While this method is suitable for field work for determining simple limits of infiltration, in laboratory settings where composition and gradients of ion concentration are desired, simple staining techniques are insufficient.

For laboratory studies where samples are soaked in potassium chloride (KCl) solutions, μXRF provides the capability of tracking both potassium and chloride ion infiltration into the concrete and examining spatial distributions with 80 μm lateral resolution while visualizing distributions over centimeter distances. Figure 5 shows side by side comparisons of Cl, K, and K, K X-ray images from a mortar sample exposed to a solution of KCl and sodium chloride (NaCl) (1 M in Cl^-, 87% KCl and 13% NaCl by mass) for over 2 months. The gradient of infiltration of chloride ions is clear in the Cl image, where the outside surface of the concrete is positioned at the top of the sample. Interestingly, the K infiltration does not appear to have gone as deeply into the concrete specimen. While most cement contains some potassium, the concentration increases toward the outside of the cylinder. The sample was not polished. The broken section was analyzed in the instrument as-is. In this case, the μXRF provided a unique method for X-ray analysis where other methods would be too difficult or would yield insufficient data. It is an example of large area mapping of extremely difficult samples for the purpose of mapping a concentration gradient that changed over the course of several millimeters.

μXRF analysis has advantages over SEM/EDS for the analysis of cement and concrete. X-ray analysis of Cl presents a special difficulty when preparing concrete samples for

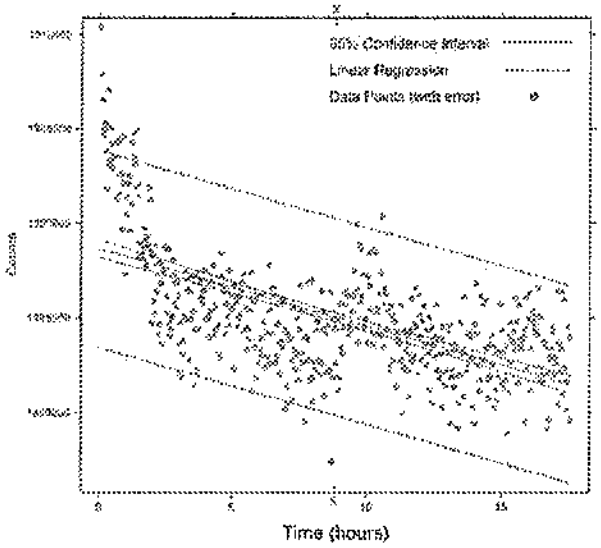

Figure 3. Signal stability measurement. This chart shows the integrated intensity (blue dots) of the Si Kα peak from 500 measurements on a single point over the course of 18 h. The magenta line represents the linear regression, with its corresponding prediction error in green. Red lines show the 95% confidence interval, defined as 2σ. Confirming the slight signal degradation over time, the linear regression has a slope of approximately −0.02% per hour. Over longer periods (>24 h), the tube will assume a steady if somewhat oscillating signal intensity, although the trend during the first 18 h is clearly negative. The tube was ramped from minimum power to near maximum power at the start of the analysis, accounting for the initial signal drop off of approximately 0.3% of the maximum signal intensity. Note that the counting and time errors are smaller than the ellipses representing single datum.

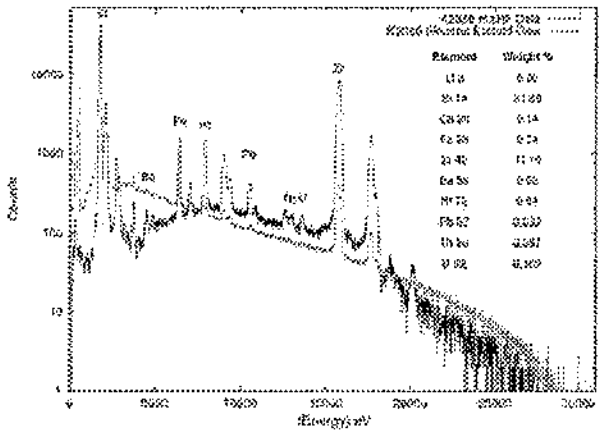

Figure 4. X-ray excited and electron excited spectra of K2380 glass. This figure shows two analyses of the same glass on a logarithmic plot. The black curve shows the analysis of the glass using 30 keV polychromatic X-rays, while the red curve shows the analysis using 30 keV electrons. The Kα peaks have been marked for reference. Note that the Lα peaks for Th and U are not present in the electron excited spectrum. Also note the higher energy behavior present in both spectra. In the electron excited case, the Duane-Hunt limit is not 30 keV, likely due to sample charging. While in the X-ray excited case, the high energy fall off is due to the capillary optics acting primarily as a shield to higher energy X-rays.

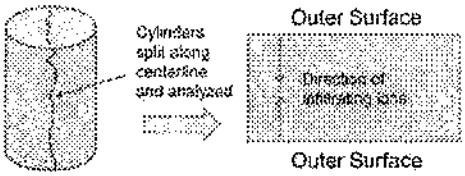

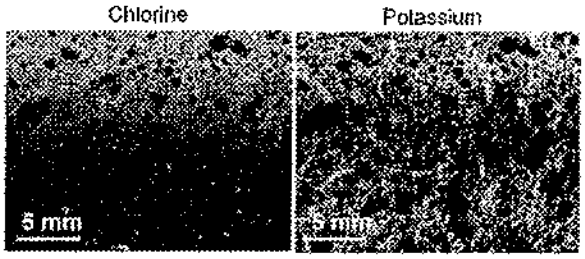

Figure 5. X-ray maps of concrete cross section. The chlorine and potassium images are shown below the concrete surface preparation graphic. Prior to analysis, the cylinders were removed from the chloride salt bath and split along the center line. A portion of the exposed surface was analyzed to see chloride and other ion infiltration. In the images shown, the outer surface (that is, the surface closest to the salt solution during soaking) is at the top of the image. The area analyzed extends from the outer surface to the approximate center of the cylinder.

analysis in an SEM. To get spatially useful X-ray data, it is necessary to polish the surface. Normal polishing requires the use of water or alcohol as a lubricant, but chloride ions are highly soluble in both liquids so the distribution is likely to be altered during polishing. The use of alternative lubricants such as mineral oil and propylene glycol may reduce the washing away of chloride ions, but such liquids are not suitable for a high vacuum environment as they are difficult to remove completely from concrete. By circumventing these difficulties, μXRF has an important advantage for cement and concrete microanalysis. First, the nature of the X-ray beam and the high take-off angle (60° compared to 40° or less for the SEM) of the EDS detector allow the user to image rough samples prepared by simple mechanical splitting without the significant shadowing that would be seen in an SEM. Second, X-ray analysis does not require even the modest vacuum of the variable pressure SEM–environmental SEM class of instruments (100 to 3,000 Pa), meaning that remaining liquids do not require drying or removal before analysis. This means that the primary elements of interest—Si, S, Cl, K, and Ca—can be detected and imaged in a system at atmospheric pressure or at modest vacuum. Although the presence of Ar, nominally about 1% by weight of air, does produce some absorption issues for analyses conducted at standard atmospheric pressure, modest vacuum along with a He backfill are usually sufficient to mitigate this effect. Third, by collecting the full X-ray spectrum at every pixel, the data can be interrogated through spectral analysis. In this case, the integral intensity of the Cl K-$L_{2,3}$ peak can be used to generate both background and peak infiltration limits for chloride ion ingress.

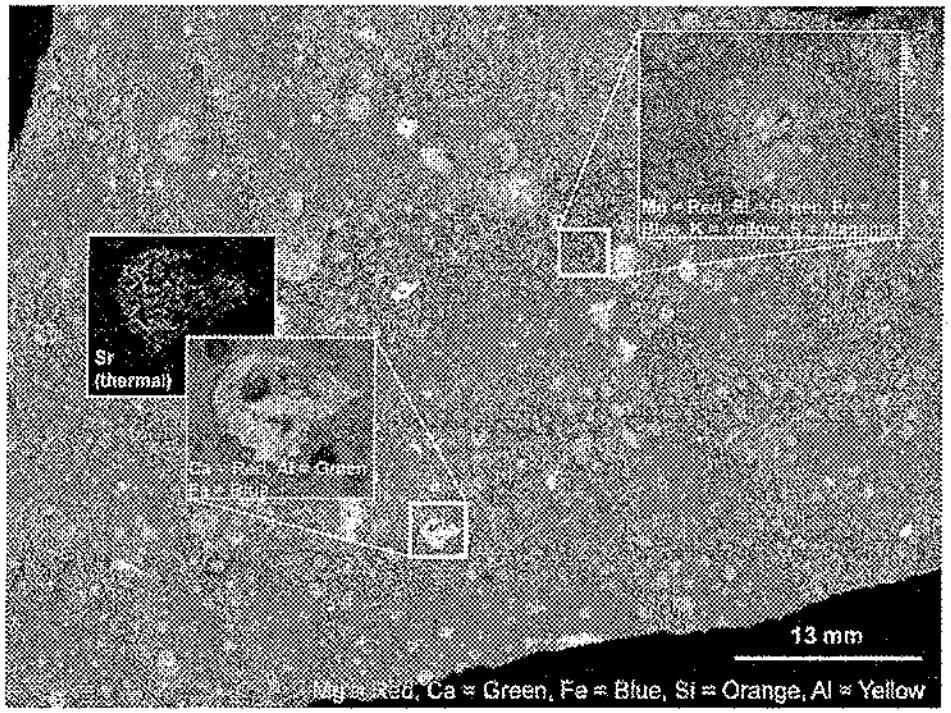

Figure 6. Color overlay of the Allende meteorite. This color overlay shows combined data from the Mg (red), Ca (green), Al (yellow), Si (orange), and Fe (blue) X-ray maps. Of particular interest in this sample were the CAIs, which can be seen as yellow-green inclusions in the iron rich matrix. The size of the grains separated out in the image range from approximately 250 μm to nearly 5 mm. Imaging grains in this size range over such a large area shows a clear application for large area μXRF imaging.

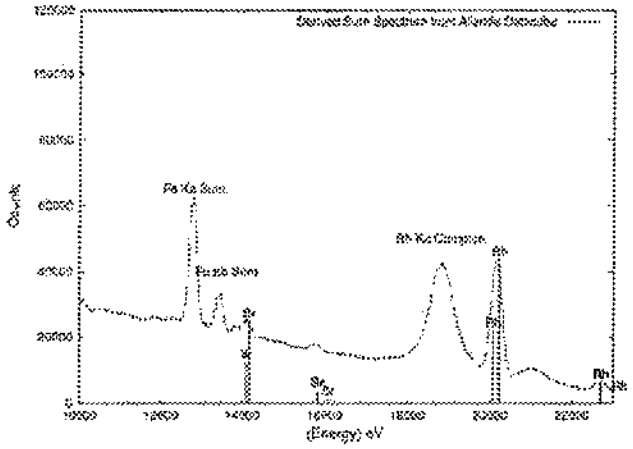

Figure 7. Derived X-ray spectra from Allende meteorite datacube. The derived spectrum from the Sr rich CAIs is shown. Although most of the specimen contains Sr well below the detection limit for XRF techniques, some of the CAIs had detectable levels of Sr. Through a user-directed searching algorithm, the pixels containing Sr were identified and summed together to produce the spectrum.

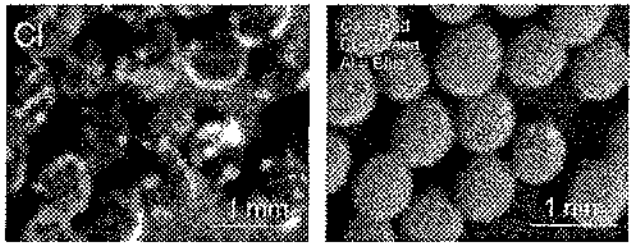

Figure 8. X-ray images of glass spheres coated in PVC. The derived X-ray images above show the distributions of elements in glass spheres. The image on the left is the Cl K-L3 image, while the image on the right is a three color overlay showing the Al K-L3 image in red, the Ca K-L3 image in blue, and the Cl K-L3 image in green. Notice that the Cl X-rays come exclusively from the exteriors of the spheres, producing a ring around each one, and the particularly high contamination in two spheres on the right side of the image.

Trace Element Imaging

An excellent example of trace element imaging comes from the earth and planetary sciences community. Meteorites are complex specimens both mineralogically and chemically. The majority of sample-based cosmochemical and planetary science studies are performed at length scales of hundreds of micrometers and smaller. Studies that make use of elemental images at the millimeter-scale through the use of stage rastering or combined stage/beam rastering (image tiling) are fewer and suffer from problems of undersampling and impractically large datasets, respectively. Both issues lead to difficulty in surveying for trace elements in large specimens.

In the following example we have examined the Allende meteorite that fell to Earth in 1969. Allende is classified as a carbonaceous chondrite, a variety of primitive meteorite. The term primitive refers to the fact that the chondritic bulk

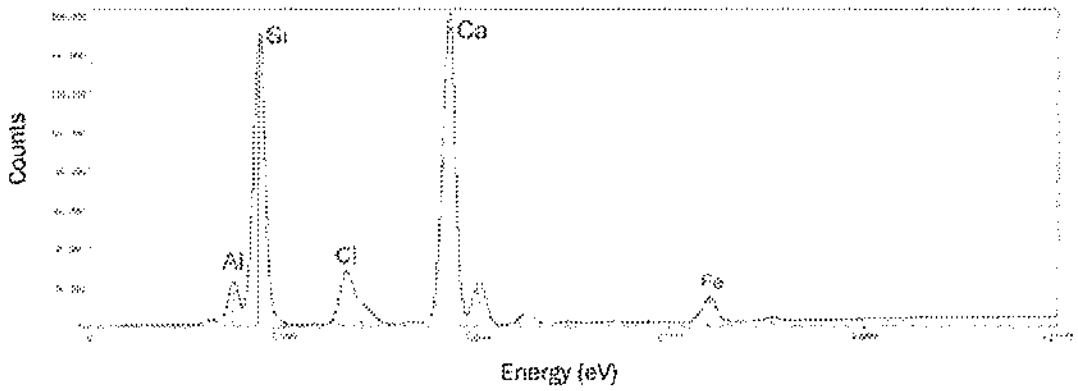

Figure 9. X-ray sum spectrum from PVC-coated spheres. The above spectrum shows the advantage of using an aluminum filter to remove scattered Rh L lines from the spectrum. The Cl peaks, normally hidden by the Compton and Rayleigh Rh peaks, are clearly visible above the background.

chemistry roughly approximates the composition of our solar system. The Allende specimen contains two types of particle assemblages that represent components from the early solar nebula, including: (1) Ca-Al-rich inclusions (CAIs), submillimeter aggregates of Ca and Al silicate and oxide minerals, and (2) chondrules, or submillimeter spheres of Mg silicates, predominantly olivine and pyroxene (Martin & Mason, 1974). In the Allende specimen, chondrules, CAIs, and FeNi metal grains are all cemented together by a fine-grained matrix of anhydrous/hydrous silicates and prebiotic organic matter.

Large-scale mapping of a polished slab measuring approximately 8 cm × 5 cm was conducted in an effort to discern both the disposition and the composition of these major components. In this experiment, the μXRF provided the advantages of both trace element sensitivity and large area mapping. Figure 6 shows that CAIs, chondrules, Fe-rich metal grains, all embedded in a silicate-rich matrix, can be distinguished by μXRF imaging through the use of simple color overlays. The lower detection limit of μXRF relative to electron-induced X-ray microanalysis also offers the ability to define areas containing trace Sr within the Ca-Al-rich inclusions.

With the information provided by the full-spectrum X-ray dataset, a meteorite researcher could, in principle, compare individual chondrules to the bulk chondrule composition without performing a physical separation. In fact, any number of compositional estimates can be made once each chemical phase has been extracted from the three-dimensional data cube. An example of such data mining and spectrum derivation is shown in Figure 7. Using NIST Lispix (Bright, 2000), the pixels whose spectra have been identified as similar through a comparison of the relative X-ray intensities in the recorded spectra were summed together and recorded as a single spectrum. Those pixels having relatively high Sr X-ray intensities were excluded from the "matrix" class (to which the majority of pixels belonged) and were summed together to form the CAI class. The resulting spectrum is displayed as Figure 7 and scaled to highlight the Sr X-ray region. This type of supervised spectral reclassification is only a small part of the advantages afforded by full hyperspectral data.

Imaging Difficult Samples

The final example of μXRF imaging shows samples that are nearly impossible to image *in situ* using electron probe methods. NIST received a series of glass spheres coated in what appeared, optically, to be an oily liquid. The μXRF proved to be particularly useful and expedient because no special sample preparation was required, and the oil could be imaged qualitatively to determine its composition. The images are shown as Figure 8, along with the sum spectrum, shown as Figure 9.

The spheres are composed primarily of typical elements that are found in a glass—Si, Al, Ca, Fe, and Ti. Operating on a suggestion that the oily film may be some form of polyvinyl chloride (PVC), an aluminum filter was selected to improve the reliability of Cl detection. With Rh targets, the Rh L edges overlap significantly with the Cl-K edges. To circumvent this, the primary X-ray beam is passed through a 25 μm thick Al foil. The Al foil is an efficient absorber of Rh L X-rays, but not of higher energy continuum X-rays. The result is that the Cl concentration can be imaged without the problem of overlap. Ultimately, the film was determined to be a form of PVC, although quantitative analysis was carried out using other instrumentation.

Suggestions for Future Development of μXRF Instrumentation

As μXRF instrumentation becomes more widely used, a series of improvements may be made to decrease the time necessary to acquire high data density X-ray images. In terms of practicality, it is best to consider how to increase sample throughput by increasing the flux of the X-ray source, and increasing the maximum count rate of the X-ray detector. High-quality imaging and quantitative analysis are largely dependent on the total integrated counts per pixel. Generally, qualitative images aim to get a few hundred counts per pixel, while quantitative images often require more than 10,000 counts. With very little change to the

geometry or operating conditions of the system, a silicon drift detector (SDD), capable of storing the required number of X-ray events four to seven times faster, will decrease sample imaging time. Even with modest X-ray sources, metallic and some geological materials are capable of saturating a Si(Li) detector past paralyzing dead time. For samples that do not fluoresce efficiently (those with low atomic number matrices), the SDD can provide enhanced detection of lower energy X-rays and improved spectral resolution, provided that the detector comes with an atmosphere supporting ultrathin window. The trade-off, however, is that the most SDDs are only 300 μm thick and therefore have much lower efficiencies for X-rays >10 keV such as Sr K_{K-L3}. An ideal system could take advantage of both detector types and include both in the system.

The second improvement could come from modifications to the source and capillary optic setup. X-ray sources with rotating anode generators, while more expensive, are the best available option for increasing the flux for laboratory source instruments. Ultimately, any change to the nature or flux of the primary radiation will necessitate a change to the capillary optics (Janssens et al., 1996). While radiation damage may be problematic for some polycapillary optics, there are still improvements to be made in terms of beam flux. In addition, a lower cost option would be to use a 1 kW source, such as those typically used in wavelength dispersive XRF analysis. A higher powered X-ray source would likely provide enough flux to fully utilize an SDD. The type of high-flux, high-speed mapping described here is already being practiced at various beam lines around the country.

Conclusion

The micro-to-macro problem can be sufficiently expressed as three fundamental problems:

1. The linear sweep of an electron beam at low magnification is not large enough to image features greater than approximately 2 mm without tiling or stage mapping.
2. Imaging large samples for the presence of trace elements often rely on undersampling, or wavelength dispersive methods.
3. Imaging large samples without *a priori* knowledge of the features or elements of interest are impractically time consuming and require analysis of extremely large datasets.

By contrast, large area μXRF mapping has three primary uses:

1. X-ray imaging of features whose length scale is centimeters or larger
2. imaging trace elements in an energy dispersive system so as to facilitate phase differentiated compositional analysis
3. scanning over comparatively large areas without *a priori* knowledge to later identify areas for further microstructural analysis.

Given the above lists, it is clear where μXRF-XSI can provide significant advantages to the microanalysis community. Specifically, large area imaging and analysis provide a useful picture of the compositional makeup of a sample. As part of a microstructural study, it is vital to know whether the areas analyzed are representative of the sample as a whole. In this way, μXRF-XSI becomes a complementary technique to microanalysis with electron or ion beam instruments.

It is important to note that accurate, efficient μXRF imaging first requires characterization of the incident radiation and of the detector. Calibrations on NIST standard reference materials or other standards, as well as routine measurements on common samples, will ensure accurate, reliable data.

References

ACI-222 (1996). *Corrosion of Metals in Concrete (ACI 222R-96).* Farmington Hills, MI: American Concrete Institute.

Adams, F., Janssens, K. & Snigirev, A. (1998). Microscopic X-ray fluorescence analysis and related methods with laboratory and synchrotron radiation sources. *J Anal Atom Spectrom* **13**, 319–331.

Boehme, D. (1987). X-ray microfluorescence of geologic materials. *Adv X-Ray Anal* **30**, 39–44.

Bright, D. (2000). Lispix: Image processing and data visualization tool for the PC and Macintosh. *Scanning* **22**, 111–112.

Carpenter, D. (1989). Improved laboratory X-ray source for microfluorescence analysis. *X-ray Spectrom* **18**, 253–258.

Carpenter, D. & Taylor, M. (1991). Fast, high resolution X-ray microfluorescence imaging. *Adv X-Ray Anal* **34**, 217–223.

Collepardi, M., Marcialis, A. & Turrizuani, R. (1970). Kinetics of penetration of chloride ions into the concrete. *Il Cemento* **4**, 157–164.

Cosslett, V. & Duncumb, P. (1956). Micro-analysis by a flying-spot X-ray method. *Nature* **177**, 1172–1174.

Gurker, N. (1986). Imaging techniques for X-ray fluorescence and X-ray diffraction. *Adv X-Ray Anal* **30**, 53–65.

Havrilla, G. (1997). Applications of micro X-ray fluorescence to materials science. *X-Ray Spectrom* **26**, 364–373.

Janssens, K., Vekemans, B., Vincze, L., Adams, F. & Rindby, A. (1996). A micro XRF spectrometer based on a rotating anode generator and capillary optics. *Spectrochem Acta B* **51**(13), 1661–1678.

Kotula, P.K., Keenan, M.R. & Michael, J.R. (2003). Automated analysis of SEM X-ray spectral images: A powerful new microanalysis tool. *Microsc Microanal* **9**(1), 1–17.

Martin, P. & Mason, B. (1974). Major and trace elements in the allende meteorite. *Nature* **249**, 333–334.

Monfore, G. & Verbeck, G. (1960). Corrosion of prestressed wire in concrete. *ACI Mater* **57**, 491–516.

Nichols, M., Boehme, D., Ryon, R., Wherry, D., Cross, B. & Aden, G. (1987). Parameters affecting X-ray microfluorescence analysis. *Adv X-Ray Anal* **30**, 45–51.

Rindby, A., Engstrom, P., Larsson, S. & Stocklassa, B. (1989). Microbeam technique for energy-dispersive X-ray fluorescence. *Adv X-Ray Spectrom* **18**, 109–112.

Ritchie, N. (2008). *DTSA II.* Retrieved from Public Domain Software Available from the NIST: http://www.cstl.nist.gov/div837/837.02/epq/dtsa2/index.html. Gaithersburg, MD: National Institute of Standards and Technology.